frontiers | Frontiers in Marine Science

TYPE Original Research
PUBLISHED 06 October 2025
DOI 10.3389/fmars.2025.1619169

OPEN ACCESS

EDITED BY
Xing Wang,
Xihua University, China

REVIEWED BY
Rodrigo Carvalho,
Rio de Janeiro Botanical Garden, Brazil
Xiang Su,
Chinese Academy of Sciences (CAS), China
Muhammad Jamil,
COMSATS University Islamabad, Pakistan

*CORRESPONDENCE
Kefu Yu
kefuyu@scsio.ac.cn
Bin Xiong
xiongbin@glut.edu.cn

RECEIVED 27 April 2025
ACCEPTED 15 September 2025
PUBLISHED 06 October 2025

CITATION
Yang Y, Yu K, Xiong B, Jiang W, Xu S, Wang R and Fan T (2025) Characteristics and primary controls of coral reef carbonate karstification in the South China Sea since the Miocene. *Front. Mar. Sci.* 12:1619169. doi: 10.3389/fmars.2025.1619169

Characteristics and primary controls of coral reef carbonate karstification in the South China Sea since the Miocene

Yang Yang[1], Kefu Yu[2,3]*, Bin Xiong[1]*, Wei Jiang[2], Shendong Xu[2,4], Rui Wang[2] and Tianlai Fan[2]

[1]Guangxi Key Laboratory of Hidden Metallic Ore Deposits Exploration, College of Earth Sciences, Guilin University of Technology, Guilin, China, [2]Guangxi Laboratory on the Study of Coral Reefs in the South China Sea, Coral Reef Research Center of China, School of Marine Sciences, Guangxi University, Nanning, China, [3]Southern Marine Science and Engineering Guangdong Laboratory (Guangzhou), Guangzhou, China, [4]Yantai Institute of Coastal Zone Research, Chinese Academy of Sciences, Yantai, China

Coral reef karstification plays a vital role in sea-air CO_2 exchange, yet its mechanisms remain unclear. This study employs an 878.22-m coral reef sequence (dating to19.6 Ma) from Well CK2 in the Xisha Islands, South China Sea (SCS), to investigate karstification processes, including their signatures, primary controls, and implications for marine carbonate dissolution in global carbon cycling. Petrological and geochemical analyses of CK2 revel distinct karstification characteristics, including: (1) higher surface porosity 25–30%), with randomly distributed pores and fractures of variable sizes and shapes; (2) yellowish-brown to black impregnations; (3) micritic cements accompanied by well-crystallized mineral crystals, and (4) moderately well-sorted and rounded grains. Geochemical signatures show elevated $^{8787}Sr/^{86}Sr$, Mn content, and Mn/Sr ratios, coupled with depleted $\delta^{13}C$, $\delta^{18}O$ and Sr content. These features collectively indicate that karstification in CK2 was dominated by non-selective dissolution and recrystallization processes, principally occurring at the mixing zone in meteoric water systems during prolonged subaerial exposure. Karstification signatures varied across geological epochs, implying different controlling mechanisms. Late Miocene (12.6–10.2 Ma), driven by sustained sea-level fall, exhibited an extreme $^{87}Sr/^{86}Sr$ shift and severe erosion. Pleistocene (2.2–1.8, 1.1–0.89, 0.29 and 0.2 Ma), influenced by frequent sea-level fluctuations and warm, humid environments linked to glacial-interglacial cycle and Asian monsoon, displayed the highest surface porosity (15–40%, mean 25%), ochre to tawny impregnations, and micritized cements, along with negative $\delta^{13}C$-$\delta^{18}O$ and elevated $^{87}Sr/^{86}Sr$ and Mn/Sr ratios. In contrast, the Middle Miocene Climatic Optimum (16.6–16 Ma) lacked typical karst characteristics but comprised of well-rounded and sorted coral gravels, suggesting reef-

building organisms mediate karstification via substrate architecture. These findings demonstrate that sea-level changes and climate conditions control coral reef karstification intensity. Concurrently, dissolution during karstification may significantly modify ocean alkalinity and dissolved inorganic carbon, with potential feedback on carbon cycling in future climate scenarios.

KEYWORDS

coral reef carbonate, karstification, meteoric diagenesis, shallowmarine carbonate dissolution, global carbon cycling, South China Sea

1 Introduction

Coral reefs represent one of Earth's most biodiverse ecosystems, accounting for 32–43% of shallow marine calcium carbonate production and playing a crucial role in global carbon cycling (Frankignoulle and Gattuso, 1993; Suzuki et al., 2001; Yan et al., 2009; 2016; Jiao et al., 2018). These ecosystems modulate atmospheric CO_2 through both calcification (CO_2 release) and dissolution (CO_2 uptake) (Berger, 1982; Berger and Keir, 1984; Opdyke and Walker, 1992; Archer et al., 2000; Fagan and Mackenzie, 2007; Purkis et al., 2010; Andersson, 2015; Lonborg et al., 2019; Yan et al., 2019). However, their dissolution contributions remain underestimated in modern carbon budgets due to the stable seawater pCO_2 conditions (Purkis et al., 2010; Andersson, 2015). The karstification of coral reef carbonate, particularly during subaerial exposure, represents a key but poorly constrained component of this carbon cycle.

Carbonate karstification requires two fundamental conditions: fluid undersaturation and continuous solute transport (Lohmann, 1988). When coral reefs are exposed during lowstands, meteoric water (equilibrated with atmospheric CO_2 but undersaturated relative to coral reef carbonate) creates distinct vertical zones of alteration under the influence of gravity and advection (Quinn and Matthews, 1990; Braithwaite and Montaggioni, 2009; Braithwaite and Camoin, 2011). The vadose zone (upper) develops typical dissolution features with sediment-filled voids (Jones, 2016; Luo et al., 2022), while the phreatic zone (middle) forms extensive cavities containing meteoric cements identifiable by their $\delta^{13}C$ and $\delta^{18}O$ signatures (Bourdon et al., 2009; Yang et al., 2022). The mixing zone (lower) exhibits especially intense water-rock interactions (Lohmann, 1988; Melim et al., 2001). These processes vary significantly with environmental conditions, showing particular sensitivity to rainfall regimes, sea level fluctuations, and monsoon activity (Melim et al., 2002; Swart, 2015; Wu et al., 2024).

Existing researches have largely focused on either contemporary reef systems or isolated ancient analogues, creating gaps in our understanding of long-term evolutionary patterns. Deep drilling of reefs carbonate sequences offers unique advantages in this regard, providing continuous records with minimal diagenetic overprinting (Schlanger and Silva, 1986; Melim et al., 2001; Yang et al., 2022; Luo et al., 2022). The SCS presents particularly valuable study sites, containing Oligocene-to-present coral reef carbonate strata exceeding 1,000 meters in thickness (Ma et al., 2011; Wu et al., 2014; Shao et al., 2017). Among them, the 928.75-m deep drilling CK2 from Yongle Atoll stands out for its exceptional recovery (> 70%) and continuity (Fan et al., 2020; Yang et al., 2022), making it ideally suited for investigating Miocene-to-present coral reef carbonate karstification processes.

This study employs an integrated petrological, geochemical, and paleontological approach to analyze multiple karstified intervals within the CK2 core. Our objectives are threefold: (1) to systematically characterize the petrological and geochemical signatures of coral reef karstification, (2) to identify the primary environmental and geological controls on these processes, and (3) to develop a comprehensive framework linking marine carbonate karstification to global carbon cycling dynamics. These findings will provide new constraints on carbonate platform evolution and its role in Earth's long-term climate regulation.

2 Materials and methods

2.1 Regional setting

South China Sea, located in the Western Pacific Warm Pool, provides optimal environmental conditions for coral reef development with its tropical climate, which are charactized by suitable sea surface temperatures (22–30 °C), high annual rainfall (1,300–2,000 mm), and suitable salinity (33.14–34.24‰). Modern coral reefs in the South China Sea cover an area of 37,935 km^2 (Figure 1A), accounting for 5% of global reef coverage (Wang et al., 2014). The Xisha Islands are located on the northwestern continental slope of the South China Sea (Figure 1A), and the development of coral reefs has been primarily controlled by tectonic subsidence and global sea-level fluctuations since the Early Miocene (Yang et al., 2022). Prolonged basement thermal subsidence has created substantial accommodation for continuous carbonate accumulation since the Early Miocene (Shao et al., 2017; Fan et al., 2020). The coral reefs in the Xisha Islands originated in the

Early Miocene; flourished horizontally, expanded to their maximum area during the Middle Miocene; contracted in the Late Miocene; and eventually evolved into isolated carbonate platforms (e.g., Yongle Atoll and Xuande Atoll) during the Pliocene and Pleistocene (Ma et al., 2011; Wu et al., 2014). The Yongle Atoll records paleoclimatic and paleoenvironmental changes since the Miocene with thick and continuous coral reef carbonate sequences (Jiang et al., 2019; Xu et al., 2019; Li et al., 2021a, b), indicating that the coral reef carbonate sequence is an ideal natural laboratory for studying the characteristics and primary controls of coral reef carbonate karstification.

CK2 was situated in a low-lying area adjacent to a sand-gravel bar on Chenhang Island, Yongle Atoll (Figure 1A). The borehole reached a total depth of 928.75 m, including 878.25 m of coral reef carbonate strata underlain by a 50.5-m volcanic basement. The carbonate sequence of CK2 consists of coral debris, reef framestones, bioclastic limestones and other reef-derived materials (Figure 1B, Fan et al., 2020). Core recovery averaged 70%, with most intervals exceeding 80%, and the cores were well-preserved as shown in Figure 1C.

The chronological framework of CK2 was established based on Strontium Isotope Stratigraphy and Magnetostratigraphy, indicates that Xisha coral reefs initiated growth at ~19.6 Ma (Figure 2A; Fan et al., 2020). Mineralogical analysis reveals distinct zonation: aragonite dominates from 0-16.9 m, calcite from 16.9–185 m and 521.4-878.22 m, mixed calcite-dolomite from 185–310 m, and dolomite from dolomite from 310-521.4 m (Figure 2A; Fan et al., 2020).

To investigate the karstification processes in the coral reefs, this study conducted a comprehensive analysis of Well CK2, including: petrological characteristics, biological composition, porosity, mineral constituents, $^{87}Sr/^{86}Sr$, $\delta^{18}O$, $\delta^{13}C$, and elemental contents. Detailed analytical informations are presented in Table 1.

2.2 Petrological and biological analysis

The petrological and biological analysis of CK2 employed a multiscale approach combining macroscopic core examination and microscopic thin-section observations.

Macroscopically, stratigraphic units were characterized through systematic documentation of: (1) sedimentological attributes (color, cementation intensity, grain-size distribution), (2) biological components content (relative proportions of skeletal debris, lithoclasts, and biotic fragments), and (3) biogenic structures (taxonomic assemblages, growth forms, and taphonomic features including mortality surfaces and dissolution pores). Diagnostic biological features were first identified in hand specimens through distinctive macro-morphological characteristics (e.g., colonial growth patterns in corals, laminar structures in microbialites).

For microscopic analysis, a systematic sampling strategy was implemented with 300 thin sections prepared at 3-meter intervals,

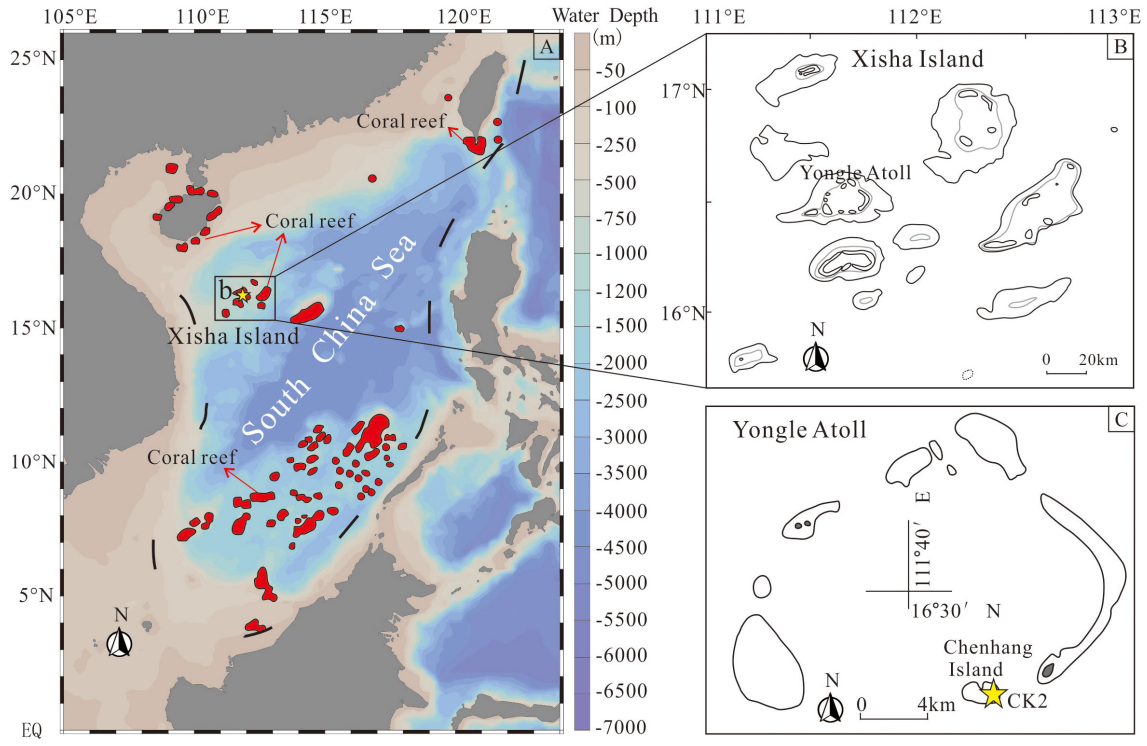

FIGURE 1
Geological map of the South China Sea and the sample location of CK2. **(A)** Map of the South China Sea Coral reef distribution (red zones, modified from Wang et al., 2014). **(B)** Map of Xisha Islands. **(C)** Map of Yongle Atoll and the location of CK2.

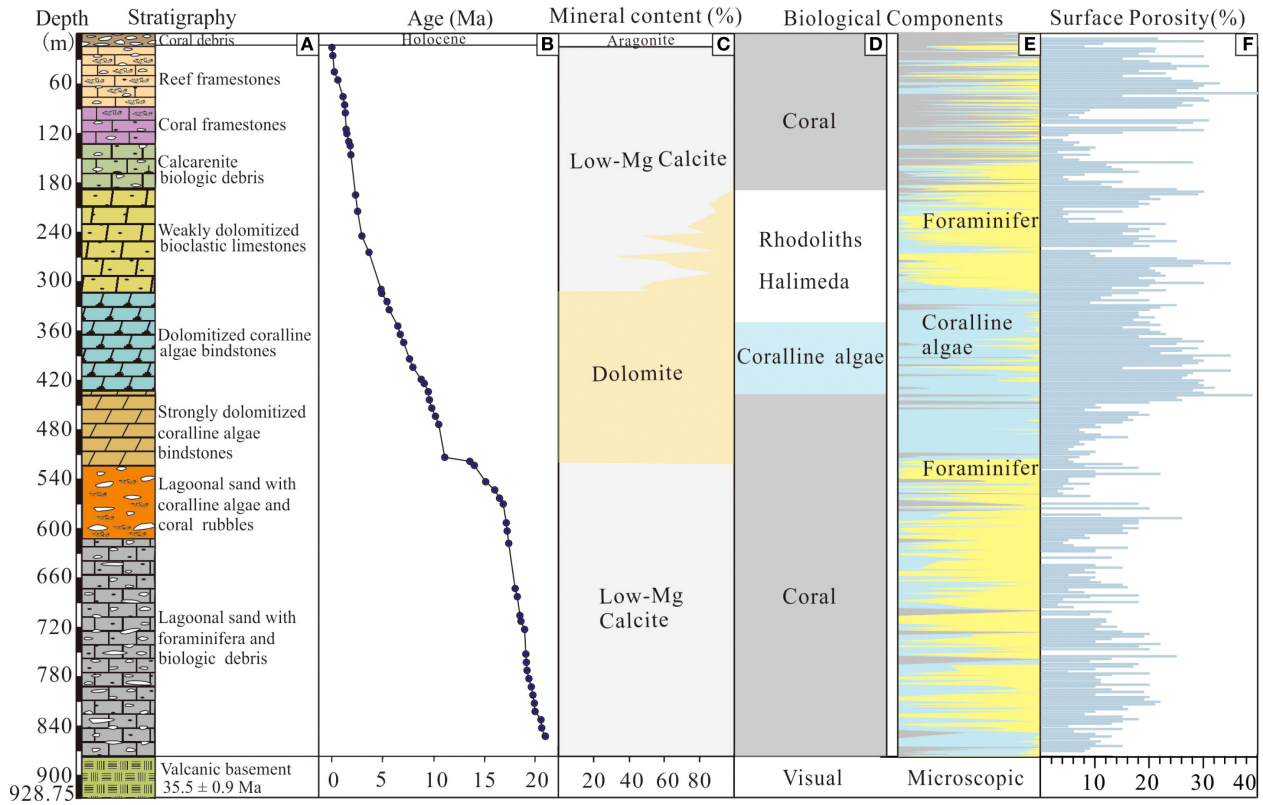

FIGURE 2
Geological characteristics of CK2: **(A)** Stratigraphy; **(B)** Chronological framework; **(C)** Mineral composition; **(D)** Visual-inspected biota; **(E)** Microscope-observed biota; **(F)** Surface porosity.

following Flügel's (2010) classification scheme. Thin sections were examined using polarized light microscopy to verify taxonomic identification through diagnostic microstructural criteria (e.g., septal arrangements in scleractinian corals, cellular networks in coralline algae) and to differentiate primary growth fabrics from secondary diagenetic features. Particular attention was given to distinguishing between: (i) *in situ* reef framework (framestones/boundstones), (ii) reworked debris (rudstones/floatstones), and (iii) matrix-supported fabrics (wackestones/packstones).

2.3 Analysis of surface porosity

Porosity was quantified through systematic areal (2D) analysis of 300 thin sections (sampled at 3-meter intervals) using polarized light microscopy and digital image processing. Pore spaces were identified by thresholding high-resolution photomicrographs (PPL/XPL), with ≥5 fields of view per sample analyzed to account for heterogeneity.

We analyzed 300 thin sections systematically collected from the 878.22-meter coral reef carbonate of CK2 at consistent 3-meter intervals to ensure statistical robustness. We followed the statistical criteria shown in Figure 3 (Scholle and Ulmer-Scholle, 2003; Zhao and Jones, 2012) for consistency with established methodologies.

2.4 Geochemical analysis

2.4.1 Sample selection and pretreatment

A total of 200 samples were selected for strontium isotope analysis, including 100 from Fan et al. (2020) and 60 from Yang et al. (2022).Samples were collected at 5–10 m, with increased sampling density (0.4–3m) for strata displaying significant geological anomalies. 1,000 samples were collected at 1 m intervals for carbon-oxygen isotope, of which 132 (15-147m) were previously published by Xu et al. (2020) and 217 (308.5–525 m) by Wang et al. (2018). Additionally, elemental content analyses for these 1,000 samples (1 m intervals) were partially reported in Fan et al. (2020) and Yang et al. (2022).

To ensure analytical precision and prevent contamination, all samples were subjected to rigorous pretreatment at the Coral Reef Research Center of Guangxi University, China. The samples were placed in conical flasks filled with deionized water and ultrasonicated for over 20 min. After 24 h, the supernatants were discarded. This washing process was repeated three times before the sediment was dried in an oven at 40 °C and ground to a powder finer than 200 mesh using an agate mortar. This study was conducted at the Coral Reef Research Centre of Guangxi University, China.

TABLE 1 Methods dataset of CK2.

Analysis objects	Number of samples	Sampling density	Method	Data sources
Petrological features	300 of thin section 878.22m core samples	3 m intervals	hand specimen microscope	This study
Biological components	300 of thin section 878.22m core samples	3 m intervals	hand specimen microscope	This study
Surface porosity	300 of thin section	3 m intervals	microscope	This study
Mineral content	100	10 m intervals	XRD	Fan et al., 2020
$^{87}Sr/^{86}Sr$	200	0.4–10 m intervals	MC-ICP-MS	Fan et al., 2020 and This study
$\delta^{18}O$ and $\delta^{13}C$	1000	1 m intervals	MAT-253	Xu et al., 2019; Wang et al., 2018; This study
Element content	1000	1 m intervals	ICP-MS	Fan et al., 2020; Yang et al., 2022; This study

2.4.2 Analysis of $^{87}Sr/^{86}Sr$

The Sr isotopic composition was measured using Nu Plasma high-resolution MC-ICP-MS at the Radiogenic Isotope Facility at the University of Queensland, Australia. First, 0.1 g of the pre-treated sample was dissolved in a sealed Teflon container using an HNO_3 +HF solution at 100 °C. The sample was centrifuged at 4000 r/min for 15 minutes, and the supernatant was collected and purified using a specific ion-exchange resin to isolate Sr. The high-purity Sr solution was dried on a hot plate and analyzed using MC-ICP-MS. Mass discrimination effects during instrumental analysis were corrected externally using an exponential function, with the $^{86}Sr/^{88}Sr$ ratio normalized to 0.1194 to standardize the $^{87}Sr/^{86}Sr$ ratio. Every four samples, mass bias corrections are applied using the standard material solution SRM987 with a $^{87}Sr/^{86}Sr$ ratio of 0.710249 ± 0.000009. In addition, 10% of the samples were retested to control the data quality.

2.4.3 Analysis of $\delta^{18}O$ and $\delta^{13}C$

The carbon and oxygen isotope analyses were performed using a Finnigan MAT-253 stable isotope ratio mass spectrometer that attached to a Fairbanks Carbonate Preparation Device at the China Coral Reef Research Center, School of Marine Sciences, Guangxi University. Approximately 20 mg of powdered samples were reacted with 100% H_3PO_4 at 75 °C to extract CO_2. Isotopic results are reported in ‰ relative to the V-PDB scale using the GBW04405 standard ($\delta^{18}O$ = -8.49‰, $\delta^{13}C$ = +0.57‰), with analytical precision of 0.08‰ for $\delta^{18}O$ and 0.03‰ for $\delta^{13}C$ (n=15). About 20% of samples were analyzed in duplicate to verify reproducibility within ±0.1‰.

2.4.4 Analysis of elemental content

Elemental content analysis was conducted using inductively coupled plasma mass spectrometry (ICP-MS) at the China Coral Reef Research Center, School of Marine Sciences, Guangxi University. The analytical procedures incorporated strict quality assurance/quality control (QA/QC) protocols, including routine blank measurements, duplicate sample analysis, and calibration with certified reference materials (GBW07129, GBW07133, GBW07135). Instrument performance was monitored through oxide ratio checks (CeO+/Ce+ <2%) and internal standardization (Rh/In/Re), ensuring measurement accuracy within ±5% uncertainty.

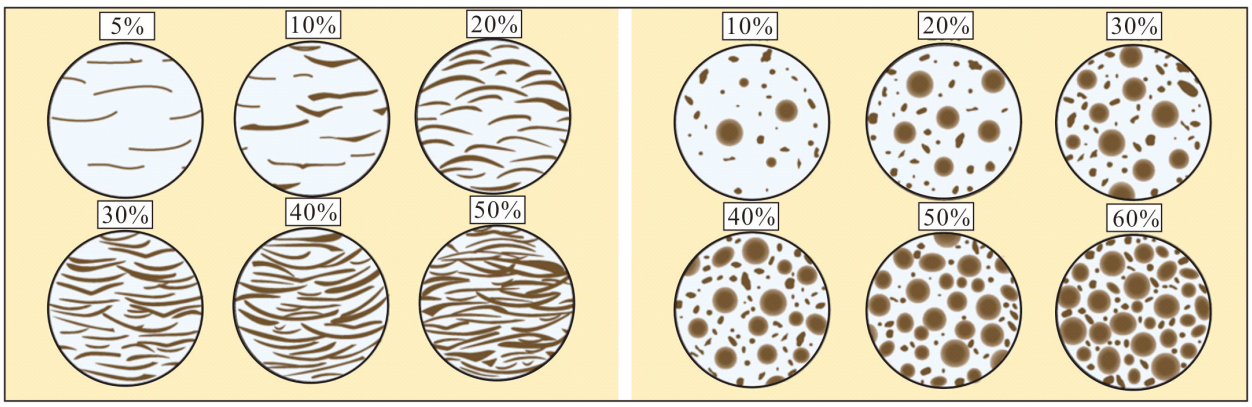

FIGURE 3
Statistical criteria for surface porosity quantification (revised based on Scholle and Ulmer-Scholle, 2003).

10.3389/fmars.2025.1619169

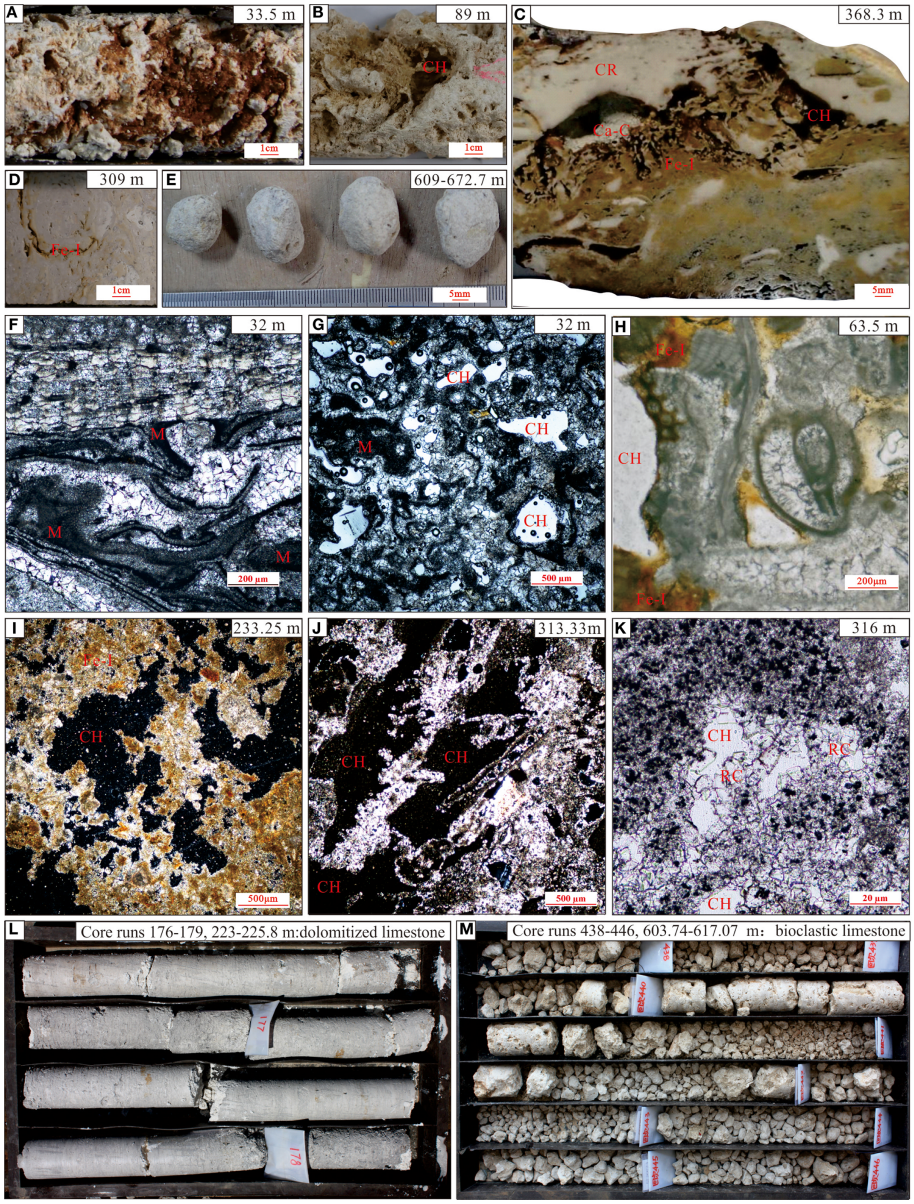

FIGURE 4
Characteristics of coral reef carbonate karstification and initial core samples in CK2: **(A–D)** Dissolution vugs and Fe-impregnated with reddish-brown calcareous crust of core samples; **(E)** Well-rounded and well-sorted coral fragments; **(F, G)** Cementation textures; **(H, I)** Dissolution pores with ferric impregnation; **(J, K)** Dissolution pores and recrystallized calcite; **(L, M)** Initial core samples. CH, corrosion cavern; CR, coral reef; M, micrite; RC, recrystallization; II, Fe infection.

3 Results

3.1 Petrological features

The CK2 core is predominantly white biogenic limestone (Figures 4L, M) that demonstrates vertical lithological variations from top to base: unconsolidated coral debris, reef framestones, coral framestones, calcarenite with biological debris, weakly dolomitized bioclastic limestones, dolomitized coralline algae bindstones, strongly dolomitized coralline algae bindstones, lagoonal sand with coralline algae and coral rubbles, and lagoonal sand with foraminifera and biological debris. These facies changes reflect gradual transitions in biological composition, mineral content, sedimentary structure, and degree of cementation.

However, distinct abnormal intervals were identified at specific depth ranges (32–34, 60.5–93.5, 190–196.7, 309–313.29, 316–320, 364–370, 413–452, 521–596, 603.7–672.74, and 831.6–834.6 m) as shown in Figure 4. These zones exhibit macroscopic features including significant color variations, (from white to yellowish, brownish-yellow, or brown-red), abundant dissolution pores/vugs lined with calcareous crusts or clayey deposits (brownish-yellow to reddish-brown and black), and occasional speleothem-like crystalline formations within well-rounded carbonate gravel. Microscopic analysis reveals: (1) irregular pores formed by

dissolution-modified biogenic skeletons by, (2) extensive micritization, (3) Fe- Mn oxide staining along pore margins, and (4) well-developed euhedral recryst crystal.

3.2 Biological composition

The CK2 reef sequence is primarily composed of corals, coralline algae, rhodoliths, Halimeda, foraminifera, and shell fragments (Figure 5). Corals occur throughout the core, with diverse taxa including Porites, Galaxea, and Acropora, but they dominate as the principal framework builders in two intervals: 0–190 m and 434.66–878.2 m. In the upper interval (0–190 m), corals mainly exist as reef framestones and rubble, while in the lower interval (434.66–611 m), they primarily form reef frameworks. Below 611 m to 878.2 m, they predominantly appear as rubble, often encrusted by coralline algae.Coralline algae constitute the second most important reef-building component after corals, chiefly represented by rhodoliths and laminar coralline algae. These are particularly abundant in 190–434.66 m (Figures 4–8), with 190–362 m dominated by rhodoliths and Halimeda beds, and 362–434.66 m dominated by rhodoliths and laminar coralline algae. Additionally, foraminifera, as accessory reef dwellers, are widely distributed throughout the core, with particularly high concentrations in 180–310 m and 525–878.22 m.

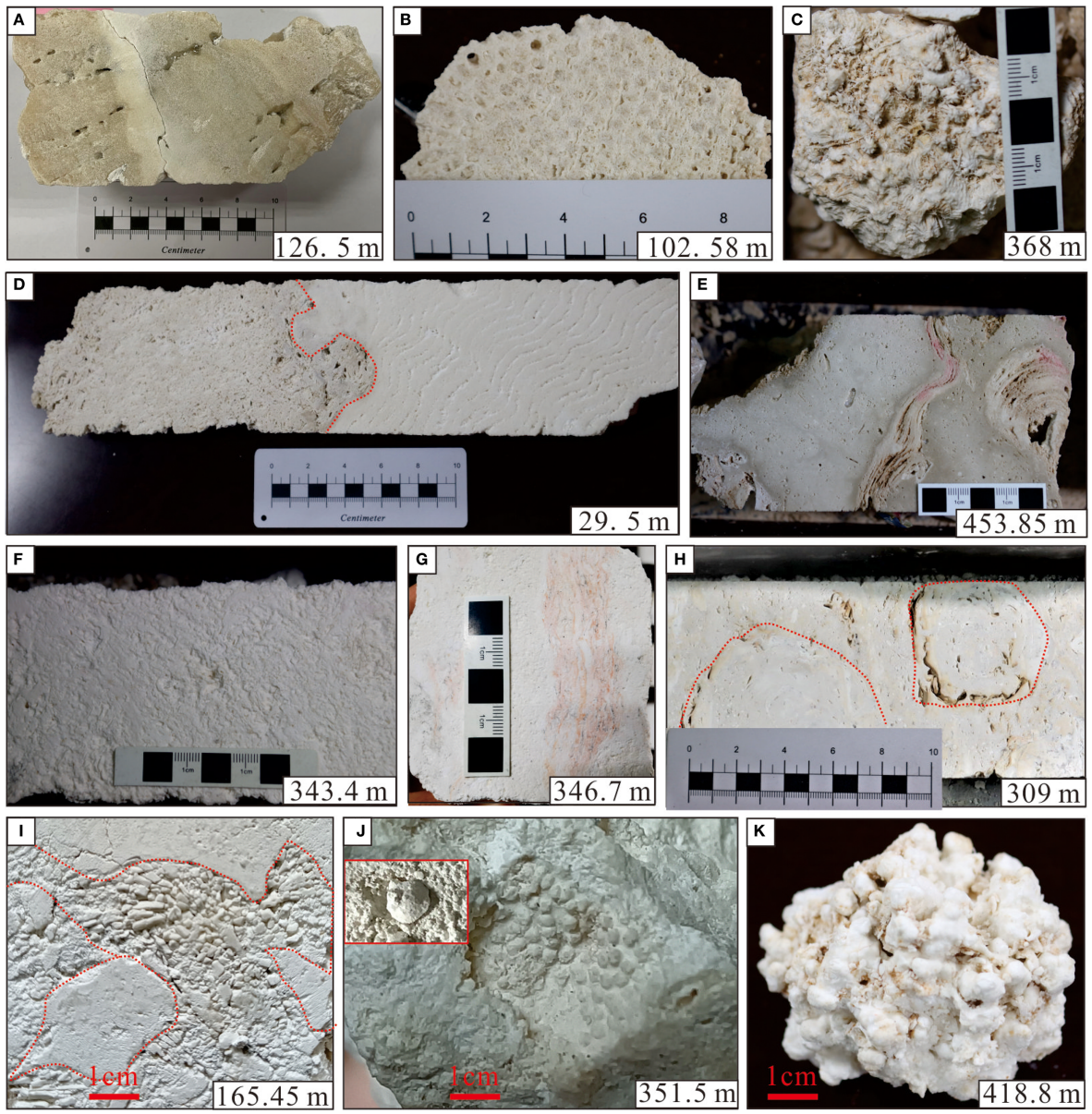

FIGURE 5
Biological composition of CK2. **(A)** Porites coral; **(B)** Galaxea coral, **(C)** Hydnophora coral, **(D)** Left: Coralline algae; Right: Porites coral, **(E)** Crustose coralline algae, **(F)** Algal nodules, **(G)** Banded coralline algae, **(H)** Rhodolith, **(I)** Halimeda, **(J)** Foraminifera, **(K)** Halimeda.

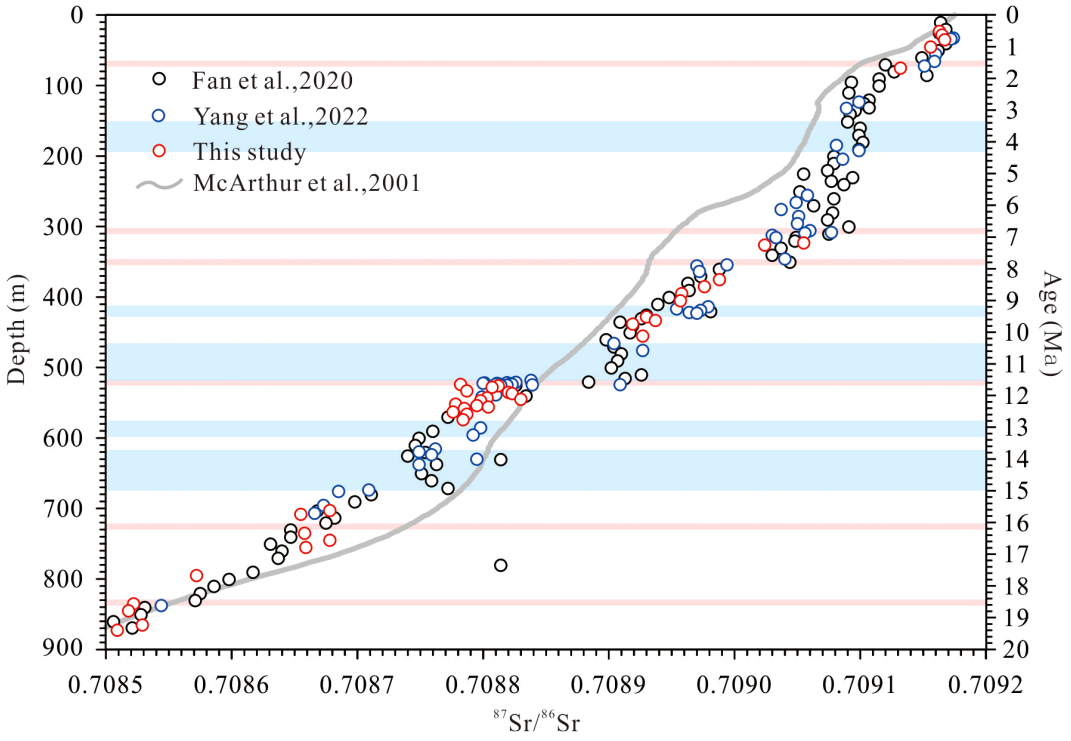

FIGURE 6
$^{87}Sr/^{86}Sr$ evolution of coral reef carbonate strata with depth of CK2 and Seawater (the circle represents the coral reef carbonate $^{87}Sr/^{86}Sr$ of CK2 and the line represents the seawater $^{87}Sr/^{86}Sr$ since 20Ma from McArthur et al., 2001).

3.3 Surface porosity

As show in Figure 2E, the surface porosity of CK2 showed a wide variation from 3 to 40% (average 16.3%), with two distinct high-porosity zones (0-90.13 m and 273.5–449 m) where most samples exceeded 20% porosity (average 24%). In contrast, lower porosity values occurred in 90-273.5 m and 449-878.22 m intervals, though with different characteristics: the 90-273.5 m section exhibited fluctuating high and low values, while the 449-878.22 m interval maintained consistently low porosity throughout.

3.4 Strontium isotopic composition

As illustrated in Figure 5 and Table 2, the $^{87}Sr/^{86}Sr$ of CK2 show a consistent secular increase from 0.708509 at the base to 0.709164 at the top, faithfully documenting the global seawater $^{87}Sr/^{86}Sr$ evolution over the past 20 Ma. However, compared to the secular evolution of seawater $^{87}Sr/^{86}Sr$, CK2 exhibit two distinct types of anomalous $^{87}Sr/^{86}Sr$ signatures: (1) positive excursions that disrupt the continuous $^{87}Sr/^{86}Sr$ progression (observed at 836–831, 731–721, 521.4–521, 354.5–351, 315–311, and 71–66 m; (2) systematically elevated $^{87}Sr/^{86}Sr$ relative to adjacent strata without observable stratigraphic breaks (occurring at 672–616, 596–575, 521–476, 423–414, and 192.5–161 m).

3.5 Stable isotopic composition and elements

The $\delta^{13}C$, $\delta^{18}O$ values and elemental contents (Mn, Sr, Mn/Sr, Al/Ti) in Well CK2 exhibit substantial variability throughout the core, which we attribute to significant mineralogical variations along the depth profile. To better characterize these geochemical anomalies, we have subdivided the stratigraphic column into four distinct mineralogical units (excluding the uppermost Holocene section from 0-16.9 m consisting of unconsolidated coral debris unaffected by diagenesis): Calcite-dominated (16.9-185m; 0.2-2Ma; 521.4-878.22m; 10.2-19.6Ma), Mixed calcite-dolomite (185-308.5m; 2-4.3Ma), Dolomite-dominated (308.5-521.4m; 4.3-10.2Ma). The systematic variations in stable isotopic compositions ($\delta^{13}C$, $\delta^{18}O$) and trace element signatures (Mn, Sr, Mn/Sr, Al/Ti) across these mineralogically-defined units are documented in Table 2 and in Figure 7.

16.9–185 m (0.2–2 Ma): $\delta^{13}C$ and $\delta^{18}O$ had a range of -6.26–0.7‰ (average: -1.86‰) and -8.67–0.42‰ (average: -1.86‰), respectively. Notably, both $\delta^{13}C$ and $\delta^{18}O$ were negative in the lowermost section (177–185 m). The concentrations of Mn and Sr were 1.73–239.42 ppm (average: 44.2 ppm) and 137.95–2381.88 ppm (average: 888.12 ppm), respectively. Throughout this unit, the Mn/Sr ratio was consistently below 0.5, with Al/Ti ranging from 3.47 to 206.54.

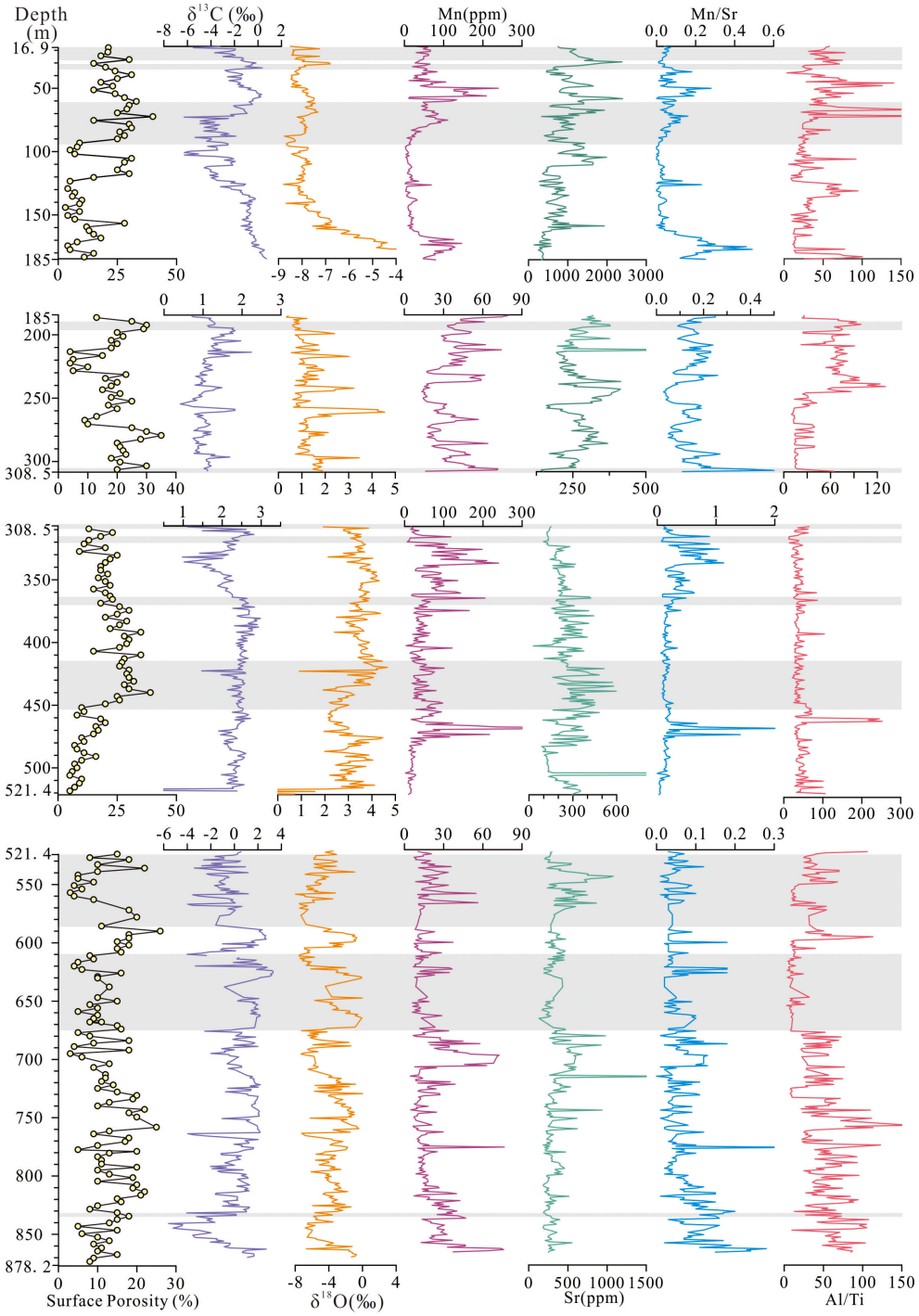

FIGURE 7
Surface porosity, δ13C, δ18O, content of Mn, Sr, and Mn/Sr, Al/Ti of each unit in CK2.

185–308.5 m (2–4.3 Ma): $\delta^{13}C$ had range of 0.41–2.24‰ (average:1.12‰), and $\delta^{18}O$ varied between 0.34‰ and 4.54‰ (average:1.39‰). Overall, $\delta^{13}C$ remained relatively stable across this interval, while $\delta^{18}O$ showed a gradual decrease upward through the unit. The concentrations of Mn and Sr were 13.33–74 ppm (average: 34.9 ppm) and 140.98–687.10 ppm (average: 272.75 ppm), respectively. The Mn/Sr ratio remained consistently below 0.5, and Al/Ti ranged from 9.75 to 130.48. Notably, the upper part of Unit 2 (186–256 m) exhibited significantly higher Al/Ti values than the lower section (256–308.5 m).

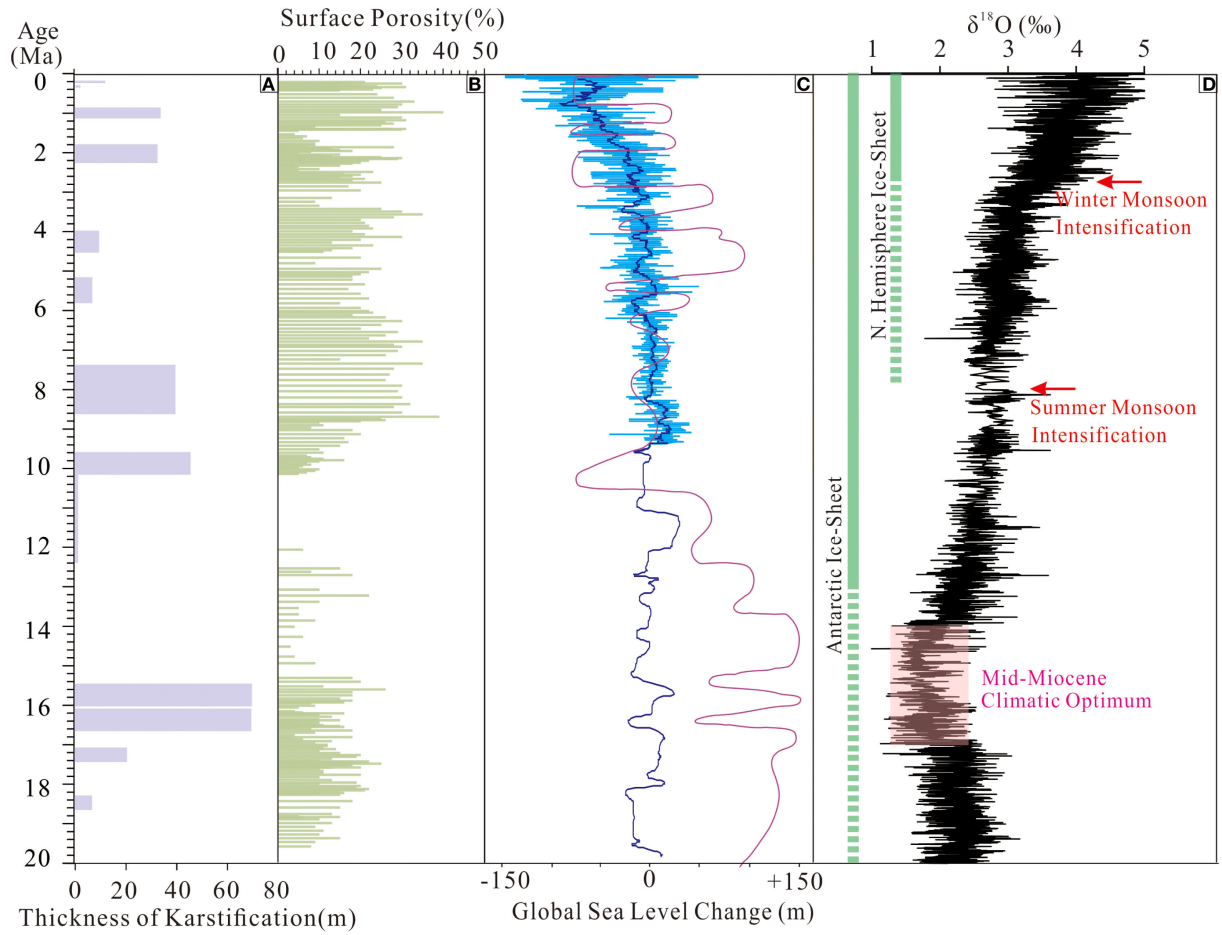

FIGURE 8
Potential control factors of the karstification in CK2. **(A)** thickness of karstification strata; **(B)** surface porosity of CK2; **(C)** sea level change since 20 Ma (Haq et al., 1987; Miller et al., 2005); **(D)** global climatic change since 20 Ma (Zachos et al., 2001, 2008).

308.5–521.4 m (4.3–10.2 Ma): $\delta^{13}C$ and $\delta^{18}O$ had a range of 0.57–2.98‰ (average: 2.22‰) and 0.71–4.66‰ (average: 2.62‰), respectively. Notably, $\delta^{13}C$ showed a significant decrease between 332–345 m, while $\delta^{18}O$ decreased in the interval 423–471 m. At the bottom of this unit (518–521.4 m), both $\delta^{13}C$ and $\delta^{18}O$ showed a negative shift. The concentrations of Mn and Sr were 2.04–237.74 ppm (average: 49.17 ppm) and 28.77–596.41 ppm (average: 299.1 ppm), respectively. Generally, Mn/Sr ratios are below 0.5, but in the intervals 321–361 m and 465–474 m, Mn/Sr had ranges of 0.55–1.13 and 0.68–2.16, respectively. Al/Ti showed a high value between 462 and 464 m (216.04–252.24), with the overall range of 12.88–105.88.

521.4–878.2 m (10.2–19.6 Ma): All data exhibited high-frequency and large fluctuations without any clear pattern. $\delta^{13}C$ ranges from -5.59‰ to 3.29‰ with an average of 0.22‰, while $\delta^{18}O$ ranged from -7.95‰ to 0.03‰ with an average of -4.03‰. The concentrations of Mn and Sr were 4.48–76.41 ppm (average: 20.1 ppm) and 130.05–1955.77 ppm (average: 361.18 ppm), respectively. Most Mn/Sr ratios were below 0.2, whereas Al/Ti ranged from 2.94 to 159.93.

4 Discussion

4.1 Characteristics of coral reef karstification

Numerous studies on carbonate platform reefs demonstrate that reef karstification predominantly occurs during lowstand (Quinn and Matthews, 1990; Luo et al., 2022; Wu et al., 2024). During reef exposure, a meteoric-marine mixing zone develops beneath the subaerial unconformity, this transitional zone, characterized by mixing of chemically distinct fluids (particularly with contrasting pCO_2 levels) and nonlinear activity coefficient behavior during solution mixing, is recognized as creating favorable conditions for the occurrence of karstification (Lohmann, 1988; Gilbert and Webster, 2015).

4.1.1 Petrological features

Core of CK2 exhibits pronounced color variations at multiple stratigraphic intervals, with distinct yellowish, brownish-yellow, and brown-red hues, which accompanied by extensive dissolution

10.3389/fmars.2025.1619169

TABLE 2 The Age, 87Sr/86Sr, δ13C, δ18O, Sr content, Mn content, Al content, Ti content, Mn/Sr ratio, and Al/Ti ratio in CK2.

Depth (m)	Age (Ma)	$^{87}Sr/^{86}Sr$ $2\sigma*10^{-6}$	$\delta^{13}C$ (‰)	$\delta^{18}O$ (‰)	Mn (ppm)	Sr (ppm)	Mn/Sr	Al (ppm)	Ti (ppm)	Al/Ti
24	0.3	0.709163±9	-1.943	-8.438	62	1232	0.05	64	1.46	43.76
29	0.3	0.709165±9	-1.088	-7.995	34	2382	0.01	37	0.74	49.76
36	0.4	0.709167±9	-2.809	-8.213	48	466	0.10	78	2.78	28.13
46	0.6	0.709156±10	-1.495	-8.345	67	1249	0.05	283	2.01	140.73
76	1.1	0.709132±10	-4.908	-7.896	85	1023	0.08	299	8.25	36.24
324	4.1	0.709055±10	2.149	3.29	102	278	0.37	350	10.51	33.25
327	5.4	0.709024±9	2.086	3.401	137	235	0.58	514	15.27	33.69
376	6.0	0.708988±9	2.68	4.106	30	187	0.16	1497	28.68	52.21
386	6.1	0.708976±9	2.902	3.276	36	281	0.13	2402	75.09	31.99
396	6.7	0.708958±9	2.522	3.396	39	398	0.10	1274	38.57	33.03
406	6.7	0.708957±10	2.51	3.566	42	261	0.16	4304	155.21	27.73
429	8.1	0.708930±8	2.278	3.755	27	219	0.12	1352	62.62	21.59
434	7.5	0.708937±8	2.536	3.936	27	250	0.11	872	22.63	38.52
439	8.8	0.708919±10	2.449	2.642	80	596	0.13	7896	265.11	29.78
456	8.4	0.708927±11	2.262	2.267	94	480	0.20	3382	47.29	71.51
525	15.0	0.708782±8	-0.039	-3.066	14	269	0.05	483	13.57	35.61
527	13.2	0.708812±8	-0.901	-5.549	7	219	0.03	798	32.48	24.58
529	13.5	0.708807±10	-2.623	-5.797	8	272	0.03	632	19.53	32.33
534	14.8	0.708787±8	-2.759	-5.293	18	387	0.05	607	15.91	38.14
536	12.9	0.708820±9	-3.406	-5.72	11	231	0.05	989	39.31	25.16
538	12.7	0.708823±11	-1.227	-4.526	22	386	0.06	644	9.22	69.86
544	13.8	0.708803±10	-0.448	-4.036	17	1010	0.02	531	14.38	36.91
546	12.3	0.708830±10	-0.857	-4.372	21	711	0.03	609	18.18	33.48
548	14.3	0.708798±10	-1.298	-5.442	9	743	0.01	650	9.55	68.02
553	15.1	0.708778±8	-1.311	-6.544	18	238	0.08	411	30.84	13.33
555	14.4	0.708795±9	-1.177	-6.581	13	419	0.03	439	45.61	9.62
557	13.7	0.708804±11	-0.679	-5.693	31	468	0.07	394	40.09	9.83
559	14.9	0.708785±9	-3.543	-7.953	10	748	0.01	250	23.57	10.62
564	15.2	0.708776±9	-0.28	-5.958	23	324	0.07	125	12.16	10.32
567	14.8	0.708787±9	-3.959	-7.513	11	344	0.03	172	13.44	12.82
575	14.9	0.708784±8	-0.397	-7.086	13	323	0.04	488	13.59	35.92
704	17.1	0.708678±9			68	577	0.12	619	21.25	29.13
709	17.4	0.708655±8	0.009	-6.462	12	595	0.02	683	24.33	28.06
736	17.3	0.708658±10			12	322	0.04	249	4.80	51.90
746	17.1	0.708678±8	2.049	-0.984	25	260	0.09	66	2.81	23.49
756	17.3	0.708659±9			21	263	0.08	79	0.50	159.93
796	18.3	0.708572±9	-1.409	-4.333	12	361	0.03	60	2.40	25.09

(Continued)

TABLE 2 Continued

Depth (m)	Age (Ma)	$^{87}Sr/^{86}Sr$ $2\sigma*10^{-6}$	$\delta^{13}C$ (‰)	$\delta^{18}O$ (‰)	Mn (ppm)	Sr (ppm)	Mn/Sr	Al (ppm)	Ti (ppm)	Al/Ti
846	19.0	0.708518±9	-4.227	-6.446	25	198	0.13	264	3.00	88.04
866	18.9	0.708529±9	0.681	-1.235	37	251	0.15	178	2.08	85.43
873	19.2	0.708509±10								

pores (Figures 4A, B). These features are even more clearly visible in cross-sectional views (Figure 4C) and microscopic observations (Figures 4H–J). This phenomenon arises when sea-level fall exposes coral reefs to subaerial conditions, allowing meteoric water infiltration that drives fluid undersaturation around reef carbonates, leading to dissolution and the formation of irregular fractures or voids. During the dissolution process, Fe and Mn become insoluble under oxidizing conditions and precipitate as hydroxides within crystalline, fibrous, and skeletal carbonates (McArthur, 1994; Butler and Rickard, 2000). Similar features have been documented in the NK-1 well of the Nansha Islands (Luo et al., 2021; Luo et al., 2022) and isolated carbonate platforms in the Pacific and Caribbean (Jones, 2016), suggesting these characteristics are diagnostic of karstification.

In addition to dissolution, the karstified carbonate strata of CK2 exhibit widespread neomorphism (Figure 4K) and various cementation textures, including meniscus, fibrous, columnar, and blocky cements (Figures 4F, G). Neomorphic alteration has been documented in Quaternary reef deposits globally, such as Australia's Great Barrier Reef, the southern Red Sea margin (Saudi Arabia), and the Huon Peninsula of New Guinea (Martin et al., 1986; McGregor and Gagan, 2003). This process is widely attributed to fluid exchange driven by meteoric freshwater infiltration and is considered characteristic of gravity-driven precipitation in the vadose zone (Braithwaite and Montaggioni, 2009; Swart and Oehlert, 2018). The calcite cementation environment shares similarities with phreatic-zone cements observed in Holocene oolitic limestones of the Bahamas (Halley and Harris, 1979; Budd, 1988).

4.1.2 Geochemical features

The geochemical composition of external fluids during karstification significantly differs from that of coral reef limestone, and their interaction can lead to the migration of chemical elements in coral reef rocks (Yang et al., 2022; Wu et al., 2024). Among these, carbon and oxygen isotopes as well as the Mn and Sr content are often used as indicators to assess the degree of diagenetic alteration in carbonate rocks.

The carbon and oxygen isotopic compositions ($\delta^{13}C$ and $\delta^{18}O$) of carbonate rocks are determined by both their original sediment composition and subsequent diagenetic alteration (Allan and Matthews, 1982). While $\delta^{18}O$ values are commonly influenced by seawater temperature and salinity (Saller and Moore, 1989; Swart and Oehlert, 2018), they can serve as reliable indicators of diagenetic processes when properly interpreted. The CK2 coral reef samples exhibit significant isotopic variability, with $\delta^{13}C$ values ranging from -6.27‰ to +4.37‰ and $\delta^{18}O$ from -8.75‰ to +4.54‰ (Figure 7). These variation correlate with mineral composition: aragonite, high-Mg calcite and dolomite show positive values with small variations, while calcite exhibits negative values with large fluctuations. To avoid the influence of minerals, we analyzed the $\delta^{13}C$ and $\delta^{18}O$ with the same mineral composition. Our results demonstrate that karst-modified layers are characterized by systematic negative shifts in both $\delta^{13}C$ and $\delta^{18}O$ values (Figure 7). These findings are consistent with previous reports from the Xisha Islands (You et al., 2015; Luo et al., 2022) and Australia's Great Barrier Reef (Braithwaite and Montaggioni, 2009), strongly supporting meteoric water alteration.

Karstification processes induce distinct geochemical alterations in carbonate rocks through interaction with Mn-enriched meteoric water (500 times the manganese concentration of seawater Mn content; Brand and Veizer, 1980). In the CK-2 karst strata, we observe three key geochemical changes: (1) increased Mn concentrations, (2) decreased Sr contents, and (3) higher Mn/Sr ratios (Figure 7). These patterns reflect characteristic of karstification: Sr is removed while Mn becomes enriched (Kaufman et al., 1993).

4.1.3 Dating of karstification in CK2

Based on the petrological and geochemical characteristics of karstified strata identified above, we recognize 11 karstification intervals in the CK2 at the following depths: 32–34, 60.5–93.5, 190–196.7, 309–313.29, 316–320, 364–370, 413–452, 521–521.4, 603.7–672.74, and 831.6–834.6 m. These intervals were dated using strontium isotope stratigraphy (SIS).

The residence time of Sr isotopes (~2.5 Myr) in the marine system far exceeds the seawater mixing time (~1000 years), resulting in globally homogeneous $^{87}Sr/^{86}Sr$ ratios in seawater (Hodell et al., 1990), this is the foundation of SIS. More precisely, the seawater $^{87}Sr/^{86}Sr$ ratio varies through geological time. By comparing the $^{87}Sr/^{86}Sr$ ratios of marine authigenic minerals (preserving original seawater signatures) with established global seawater curves, we can accurately determine sample ages (Burke et al.,1982; Depaolo and Ingram, 1985; McArthur, 1994). Coral skeletons, being biogenic carbonates, directly record seawater $^{87}Sr/^{86}Sr$ compositions upon formation, making SIS ideal for dating reef deposits. Notably, periods exhibiting rapid seawater $^{87}Sr/^{86}Sr$ variations yield higher dating resolution. Over the past 20 Myr, seawater $^{87}Sr/^{86}Sr$ has experienced a sustained increasing trend (McArthur et al., 2001; Prokoph et al., 2008), allowing for highly precise age constraints (~0.2 Ma)—particularly advantageous for constraining karstification timing.

The measured $^{87}Sr/^{86}Sr$ ratios in this study (0.708509-0.709167) show excellent agreement with previously published CK2 data from adjacent horizons (Fan et al., 2020; Yang et al., 2022; Figure 6), confirming the reliability of the chronological framework based on SIS. By constraining the ages at the upper and lower boundaries of karstified strata, we determined the timing of karstification events in CK2 to occur at: 0.3 Ma (32–34 m), 0.7-1.2 Ma (60.5-93.5 m), 2.2 Ma (190-196.7 m), 4.2 Ma (309-313.29 m), 4.5 Ma (316–320 m), 6.1 Ma (364–370 m), 7.5-8.85 Ma (413–452 m), 10.2-12.4 Ma (521-521.4 m), 15.9-16.6 Ma (603.7-672.74 m), and 18.3-18.8 Ma (831.6-834.6 m).

4.2 The primary control factors of karstification in coral reef carbonate

Karstification is a complex geological process governed by multiple controlling factors closely associated with sea-level fluctuations, climatic conditions, and biological activities. This study specifically focused on exploring the controlling mechanisms of sea level change, climatic variability, and biological factors in coral reef carbonate karstification.

4.2.1 Influence of sea-level fluctuations

Sea-level fluctuations are critical in controlling coral reef karstification across different timescales. The global sea level has dropped repeatedly (Haq et al., 1987; Miller et al., 2005) due to global cooling since 20 Ma (Zachos et al., 2001, 2008), triggering multiple karstification episodes in CK2 (Yang et al., 2022). The most pronounced sea level drop occurred during the Late Miocene as an Antarctic permanent ice sheet formed, with a >100 m sea level fall over 4 Ma (Haq et al., 1987; Miller et al., 2005). The prolonged regression triggered extensive denudation of coral reef carbonate in CK2, resulting in an $^{87}Sr/^{86}Sr$ shift from 0.708884 at 521 m to 0.708826 at 521.4 m (Figure 6), which indicates complete erosion of coral reef deposits between 12.6 and 10.2 Ma. In contrast, sea levels in the Pleistocene were characterized by rapid, high-amplitude oscillations (Miller et al., 2005) under the interglacial cycles (Zachos et al., 2001). The corresponding karst intervals in CK2 (2.2–1.8, 1.1–0.89, 0.29, and 0.2 Ma) display prominent features of karstification without stratigraphic gaps, such as high surface porosity (15–40%, avg. 25%; Table 1, Figure 7), dissolution pores with yellow-brown staining (Figures 4A, B, G, H), micritized cements (Figure 4F), and depleted of $\delta^{13}C$ and $\delta^{18}O$, elevated $^{87}Sr/^{86}Sr$ and Mn/Sr. These contrasting features of karstification during the Late Miocene and Pleistocene highlight the magnitude and duration of sea-level changes affecting the intensity and expression of karstification and imply the importance of climate on karstification.

4.2.2 Influence of climatic conditions

Climatic conditions exert an equally significant control on karstification as sea level changes, with warm-humid climates notably enhancing carbonate dissolution rates during prolonged subaerial exposure (Gaillardet et al., 2019; Mujalli et al., 2019). CK2 is located in the northern South China and is perennially influenced by the East Asian Monsoon (Jiang et al., 2019). The East Asian summer monsoon is mainly characterized by warmth and humidity, which can accelerate the Meteoric Diagenesis of coral reef carbonates (Wu et al., 2024). The Al/Ti ratio has been established as a robust proxy for variations in monsoon intensity (Jiang et al., 2019). The Pleistocene karst intervals in CK2 (2.2–1.8, 1.1–0.89, 0.29, and 0.2 Ma) exhibited significantly elevated Al/Ti ratios (Figure 8), providing direct geochemical evidence that enhanced East Asian monsoon conditions actively promoted karstification during these periods.

4.2.3 Influence of other factors

Temperatures during the Mid-Miocene Climatic Optimum (MMCO) are approximately 3-4 °C higher than today (Rohling et al., 2021). Theoretically, warm and humid climate are more conducive to carbonate minerals dissolution, suggesting that karstification in the CK2 section should have been intense during this period. However, karstified strata deposition during 16.6–16.0 Ma (603.7–672.74 m) exhibit three distinctive characteristics: (1) absence of typical karst features such as dissolution pores and Fe-Mn contamination, with surface porosity <10% (Figures 2 and 4); (2) composition of well-rounded and well-sorted gravels derived from coral skeletons (Figure 4E); and (3) normal $\delta^{13}C$, $\delta^{18}O$ and Mn/Sr ratios (Figure 7) but significantly higher $^{87}Sr/^{86}Sr$ values compared to adjacent strata (Figure 6). These features indicate the gravels were not altered by meteoric water but contain terrigenous contaminants, suggesting they represent allochthonous deposits that underwent prolonged transport before final deposition in the CK2 sequence.

As shown in Figures 2 and 5, hand specimen analysis revealed that the interval at 603.7–672.74m are predominantly composed of shallow-water corals, while the matrix consists primarily of deep-water foraminifera; microscopic examination further demonstrated a distinct bioclast assemblage, with foraminifera showing the highest abundance, followed by coralline algae, while corals were least prevalent (Li et al., 2021a, b). This indicates that the coral reef carbonate (603.7–672.74 m) primarily developed in a deep-water lagoon environment. During sea-level fall, coral reef strata in shallow reef flats were exposed to karstification, and some of the coral skeletons were prolonged by wind and waves, resulting in well-rounded and well-sorted gravel blocks, ultimately redeposited in deeper lagoon settings. This reconstruction of 16.6–16 Ma karstification highlights differential reef-building functions: coral frameworks formed through algal binding created primary structures, while foraminifera and other reef-dwelling organisms infilled voids. The resulting mesh-like framework collapsed during lowstand exposure, where currents winnowed foraminifera-rich matrix and reworked residual corals into rounded clasts, explaining both the high textural maturity and exceptionally low core recovery rates (5-10%).

In summary, the karstification process of coral reef carbonates in CK2 is controlled by multiple interdependent factors: the magnitude and duration of global sea-level fluctuations establish fundamental conditions, East Asian monsoon variability provides

climatic dynamic forcing, and reef-building organism types affect specific rock fabric evolution. This comprehensive analytical framework offers new perspectives on karst processes in paleo marine environments.

4.3 The potential impact of coral reef karstifification on the carbon cycle

4.3.1 The potential impact of karstifification in theory

This study documents that coral reef karstification represents an exceptionally intense geological process driven by the combined effects of sea-level fluctuations, climatic conditions, and biological factors. Most karstified strata of CK2 are characterized by extensive dissolution pores and fractures (Figure 4), exhibiting significantly higher porosity than adjacent strata, surface porosity typically ranges between 25% and 30% (Figure 2F), indicating that dissolution is the dominant diagenetic process in reef karstification.

Dissolution, the dominant diagenetic process, can be classified into selective dissolution and non-selective dissolution (Lohmann, 1988; Qu et al., 2013). Selective dissolution occurs during early diagenesis on a small scale, where varying solubilities of biogenic minerals (e.g., aragonite in reef-building corals, high-Mg calcite in foraminifera, echinoderms, and red algae) lead to preferential dissolution of specific components, creating biomorphic pores (Figures 9A, B); non-selective dissolution takes place after diagenesis, where metastable minerals (e.g., aragonite and high-Mg calcite) transform into stable low-Mg calcite (Figures 9A, C) and undergo large-scale dissolution under favorable conditions, forming irregular dissolution pores (Figure 9D, Wolf, 1973; Schroeder and Purser, 2012).

The karstified strata in CK2 predominantly exhibit non-selective dissolution features, including irregular cavities, neomorphic textures, and diverse cements (meniscus, fibrous, columnar, and blocky; Figure 4). These characteristics, coupled with synchronous $\delta^{13}C$-$\delta^{18}O$ depletion trends (Figure 7), closely resemble mixing-zone diagenetic patterns observed in other global reef systems, such as Enewetak Atoll, Cayman Islands and Bahamas Bahamian reefs (Saller and Moore, 1989; Melim et al., 2001; Jones, 2016). This suggests preservation of only the lower meteoric mixing zone due to complete erosion of upper vadose and phreatic zones during prolonged exposure. Supporting evidence comes from $^{87}Sr/^{86}Sr$ hiatuses at six depth intervals (836-831, 731-721, 521.4-521, 354.5-351, 31.5-311, and 71–66 m; Figure 6), which record missing sequences as demonstrated by Yang et al. (2022). Carbonate dissolution in marine environments increases the alkalinity and dissolves inorganic carbon content of seawater at a ratio of 2:1 (Archer et al., 2000; Martin, 2017; Peya, 2017). Thus, vigorous karstification of coral reef carbonate during lowstand could generates a substantial significant climate feedback mechanism.

4.3.2 Theory validation during the geological time

Based on the hypothesis, we evaluated the potential impacts of coral reef karstification on the global carbon cycle under glacial–interglacial cycles during the Pleistocene. Coral reefs were exposed to subaerial conditions during glacial periods with lower sea levels, and undergoing intense chemical weathering under the influence of the intensified East Asian monsoon, resulting in the dissolution of large amounts of carbonates and increased capacity for atmospheric CO_2 uptake, which may strengthen the global cooling trend. Conversely, sea level rise promoted new reef growth and carbonate deposition during interglacial periods, releasing CO_2 into the atmosphere and contributing to climatic warming. This dual regulatory mechanism of coral reefs in response to global climate change during glacial-interglacial cycles has been confirmed by modeling studies and is referred to as the “coral reef hypothesis” (Berger, 1982; Berger and Keir, 1984; Opdyke and Walker, 1992).

Similarly, the prolonged sea level fall caused by the formation of permanent Antarctic ice sheets during the Late Miocene exposed extensive reef carbonates to karstification. The resulting large-scale carbonate dissolution strengthened oceanic CO_2 absorption,

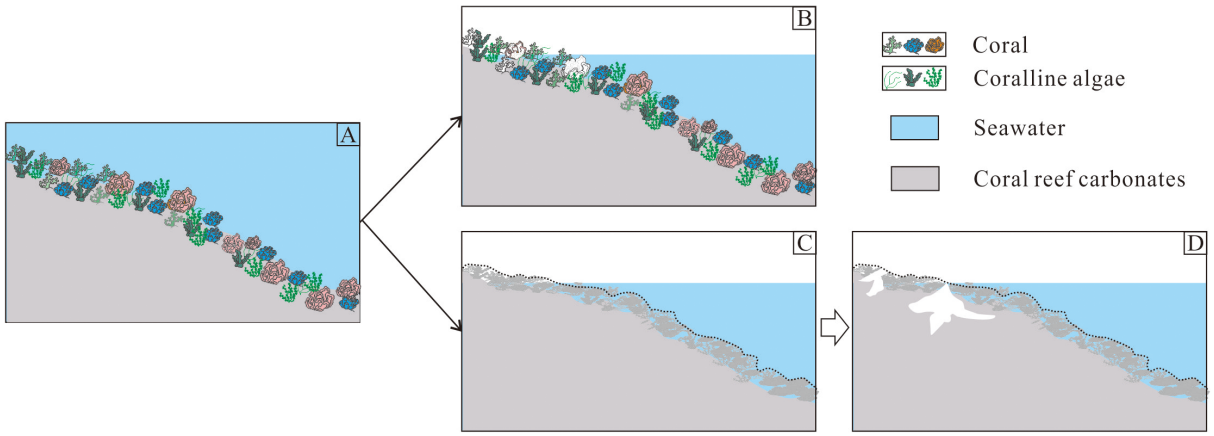

FIGURE 9
Conceptual model of coral reef carbonate dissolution: **(A)** Pristine reef structure; **(B)** Selective dissolution phase; **(C)** Diagenetically altered formation; **(D)** Non-selective dissolution stage.

reinforcing global cooling. Moreover, karstification of coral reefs remained active under warm-humid conditions and the influence of easily collapsed reef carbonate structures, MMCO, which might have partially offset the extreme warmth of this period by enhancing CO_2 uptake. These findings demonstrate that coral reef karstification operates as a dynamic feedback mechanism in the carbon cycle, capable of either amplifying or mitigating climate change depending on environmental context. Future research must quantify these effects to better constrain their roles in past and future climate transitions.

4.3.3 Prediction the impact in the future

Since the Industrial Revolution, rising global temperatures (Pörtner et al., 2022) and ocean acidification—driven by anthropogenic CO_2 emissions—have significantly altered carbon cycling in coral reef ecosystems (Andersson, 2015). These dual stressors suppress coral calcification rates while accelerating chemical dissolution and bioerosion, potentially shifting reefs from net carbonate accumulation to net loss. Such a transition could generate negative climate feedbacks by increasing oceanic alkalinity and enhancing CO_{22} uptake, albeit at the cost of reef structural integrity.

These dynamics highlight the Anthropocene's paradoxical scenario: while coral reef degradation could transiently mitigate climate change through enhanced carbon sequestration, the permanent loss of these biodiverse ecosystems would irrevocably compromise marine biodiversity and coastal protection services. Consequently, understanding reef-carbonate feedbacks remains vital for predicting both oceanic chemical trajectories and ecosystem responses to ongoing global change.

5 Conclusion

Integrated petrological and geochemical analyses of CK2 reveal that coral reef carbonate karstification is dominated by non-selective dissolution, primarily occurring in the meteoric water mixing zone during prolonged subaerial exposure. The karstified strata exhibit high porosity, dissolution pores/fractures, yellowish-brown to black impregnations, micritic cements, well-crystallized minerals, and moderately sorted grains, alongside elevated $^{87}Sr/^{86}Sr$ and Mn but depleted $\delta^{13}C$, $\delta^{1818}O$, and Sr. Three interdependent drivers govern CK2's reef carbonate karstification: global eustasy (duration/magnitude) creates the foundational framework, East Asian monsoons supply climatic forcing, and reef organisms directly shape dissolution patterns through fabric development. The study reveals that coral reef karstification-induced carbonate dissolution in shallow marine environments plays a dual role in climate evolution, as it differentially regulates ocean alkalinity a

Data availability statement

The original contributions presented in the study are included in the article/supplementary material. Further inquiries can be directed to the corresponding author.

Author contributions

YY: Conceptualization, Writing – review & editing, Software, Methodology, Funding acquisition, Visualization, Writing – original draft, Project administration, Formal analysis. KY: Resources, Validation, Project administration, Supervision, Writing – review & editing, Funding acquisition, Conceptualization. BX: Conceptualization, Writing – review & editing, Supervision. WJ: Methodology, Supervision, Writing – review & editing, Investigation. SX: Writing – review & editing, Supervision, Validation, Methodology. RW: Writing – review & editing, Supervision, Methodology. TF: Writing – review & editing, Supervision, Methodology.

Funding

The author(s) declare financial support was received for the research and/or publication of this article. This work was funded by the National Science Foundation of China (No. 42030502), Guangxi Science and Technology Program (No. AD25069075), Guangxi Laboratory on the Study of Coral Reefs in the South China Sea Open project (No. GXLSCRSCS2023002), and Fundamental Research Capacity Enhancement Program for Guangxi Higher Education Institutions Young and Middle-aged Teachers in 2025 (Grant Nos. 2025KY0305).

Conflict of interest

The authors declare that the research was conducted in the absence of any commercial or financial relationships that could be construed as a potential conflict of interest.

The author(s) declared that they were an editorial board member of Frontiers, at the time of submission. This had no impact on the peer review process and the final decision.

Generative AI statement

The author(s) declare that no Generative AI was used in the creation of this manuscript.

Any alternative text (alt text) provided alongside figures in this article has been generated by Frontiers with the support of artificial intelligence and reasonable efforts have been made to ensure accuracy, including review by the authors wherever possible. If you identify any issues, please contact us.

Publisher's note

References

Allan, J. R., and Matthews, R. K. (1982). Isotope signatures associated with early meteoric diagenesis. *Sedimentology* 29, 797–817.

Andersson, A. J. (2015). A fundamental paradigm for coral reef carbonate sediment dissolution. *Front. Mar. Sci* 2, 52. doi: 10.3389/fmars.2015.00052

Archer, D., Winguth, A. M., Lea, D. W., and Mahowald, N. (2000). What caused the glacial/interglacial pCO2 cycles? *Rev. Geophys.* 38, 159–189.

Berger, W. H. (1982). Increase of carbon dioxide in the atmosphere during deglaciation: the coral reef hypothesis. *Naturwissenschaften* 69, 87–88. doi: 10.1007/BF00441228

Berger, W. H., and Keir, R. S. (1984). "Glacial-Holocene changes in atmospheric CO_2 and the deep-sea record," in *Climate Processes and Climate Sensitivity*. Eds. J. E. Hansen and T. Takahashi (AGU, Washington, D.C.), 337–351.

Brand, U., and Veizer, J. (1980). Chemical diagenesis of a multicomponent carbonate system; 1, trace elements. *J. Sediment. Petrol.* 50, 1219–1236. doi: 10.1306/212F7BB7-2B24-11D7-8648-000102C1865D

Bourdon, B., Bureau, S., Andersen, M. B., Pili, E., and Hubert, A. (2009). Weathering rates from top to bottom in a carbonate environment. *Chem. Geol.* 258, 275–287. doi: 10.1016/j.chemgeo.2008.10.026

Braithwaite, C. J. R., and Camoin, G. F. (2011). Diagenesis and sea level changes: lessons from Moruroa, French Polynesia. *Sedimentology* 58, 259–284. doi: 10.1111/j.1365-3091.2010.01182.x

Braithwaite, C. J. R., and Montaggioni, L. F. (2009). The Great Barrier Reef: a 700–000 year diagenetic history. *Sedimentology* 56, 1591–1622. doi: 10.1111/j.1365-3091.2008.00982.x

Budd, D. A. (1988). Petrographic products of freshwater diagenesis in Holocene ooid sands, Schooner Cays, Bahamas. *Carbonates. Evaporites.* 3, 143–163. doi: 10.1007/BF03175114

Burke, W. H., Denison, R. E., Hetherington, E. A., Koepnick, P. B., Nelson, H. F., and Otto, J. B. (1982). Variation of seawater $^{87}Sr/^{86}Sr$ throughout Phanerozoic time. *Geology* 10, 516–519. doi: 10.1130/0091-7613(1982)10<516:VOSSTP>2.0.CO;2

Butler, I. B., and Rickard, D. (2000). Framboidal pyrite formation via the oxidation of iron (II) monosulfide by hydrogen sulphide. *Geochim. Cosmochim. Acta* 64, 2665–2672. doi: 10.1016/S0016-7037(00)00387-2

Depaolo, D. J., and Ingram, B. L. (1985). High-resolution stratigraphy with strontium isotopes. *Science* 227, 938–941. doi: 10.1126/science.227.4689.938

Fagan, K. E., and Mackenzie, F. T. (2007). Air-sea CO2 exchange in a subtropical estuarine-coral reef system, Kaneohe Bay, Oahu, Hawaii. *Mar. Chem.* 106, 174–191. doi: 10.1016/j.marchem.2007.01.016

Fan, T. L., Yu, K. F., Zhao, J. X., Jiang, W., Xu, S. D., Zhang, Y., et al. (2020). Strontium isotope stratigraphy and paleomagnetic age constraints on the evolution history of coral reef islands, northern South China Sea. *Geol. Soc. America Bull.* 132, 803–816. doi: 10.1130/B35088.1

Flügel, E. (2010). *Microfacies of carbonate rocks, analysis, interpretation and application* (Berlin: Springer-Verlag), 984.

Frankignoulle, M., and Gattuso, J. P. (1993). "Air-sea CO2 exchange in coastal ecosystems," in *Interactions of C, N, P and S Biogeochemical Cycles and Global Change*. Eds. R. Wollast, F. T. Mackenzie and L. Chou (Springer, Berlin, Heidelberg), 233–248.

Gaillardet, J., Calmels, D., and Romero-Mujalli, G. (2019). Global climate control on carbonate weathering intensity. *Chem. Geol.* 527, 118762. doi: 10.1016/j.chemgeo.2018.05.009

Gilbert, F. C., and Webster, J. M. (2015). Coral reef response to Quaternary sea-level and environmental changes: State of the science. *Sediment. Geol.* 62, 401–428.

Halley, R. B., and Harris, P. M. (1979). Fresh-water cementation of a 1,000-year-old oolite. *J. Sediment. Petrol.* 49, 969–987.

Haq, B. U., Hardenbol, J., and Vail, P. R. (1987). Chronology of fluctuating sea levels since the Triassic. *Science* 235, 1156–1167. doi: 10.1126/science.235.4793.1156

Hodell, D. A., Mead, G. A., and Mueller, P. A. (1990). Variation in the strontium isotopic composition of seawater (8 Ma to present): Implications for chemical weathering rates and dissolved fluxes to the oceans. *Chem. Geol.* 80, 291–307. doi: 10.1016/0168-9622(90)90011-Z

Jiang, W., Yu, K. F., Fan, T. L., Xu, S.D., Wang, R., Zhang, Y., et al. (2019). Coral reef carbonate record of the Pliocene-Pleistocene climate transition from an atoll in the South China Sea. *Mar. Geol.* 411, 88–97. doi: 10.1016/j.margeo.2019.02.006

Jiao, N. Z., Liang, Y. T., Zhang, Y. Y., Liu, J. H., Zhang, Y., Zhang, R., et al. (2018). Carbon pools and fluxes in the China Seas and adjacent oceans. *Sci China Earth Sci.* 61, 1535–1563. doi: 10.1007/s11430-018-9190-x

Jones, B. (2016). Cave-fills in Miocene-Pliocene strata on Cayman Brac, British West Indies: Implications for the geological evolution of an isolated oceanic island. *Sediment. Geol.* 341, 70–95. doi: 10.1016/j.sedgeo.2016.05.001

Kaufman, A. J., Jacobsen, S. B., and Knoll, A. H. (1993). The vendian record of Sr and C isotopic variations in seawater: implications for tectonics and paleoclimate. *Earth Planet Sci. Lett.* 120, 409–430. doi: 10.1016/0012-821X(93)90254-7

Li, Y. Q., Yu, K. F., Bian, L. Z., Fan, T. L., Wang, R., Jiang, W., et al. (2021a). Paleo-water depth variations since the Pliocene as recorded by coralline algae in the South China Sea. *Palaeogeogr. Palaeoclimatol. Palaeoecol.* 562, 110107. doi: 10.1016/j.palaeo.2020.110107

Li, Y. Q., Yu, K. F., Bian, L. Z., Qin, Y. M., Liao, W. H., Yang, Y., et al. (2021b). Coralline algal assemblages record Miocene sea-level changes in the South China Sea. *Palaeogeogr. Palaeoclimatol. Palaeoecol.* 584, 110673.

Lohmann, K. C. (1988). "Geochemical patterns of meteoric diagenetic systems and their application to studies of paleokarst," in *Paleokarst*. Eds. N. P. James and P. W. Choquette (Springer, New York, NY).

Lonborg, C., Calleja, M. L., Fabricius, K. E., Smith, J. N., and Achterberg, E. P. (2019). The Great Barrier Reef: A source of CO_2 to the atmosphere. *Mar. Chem.* 210, 24–33. doi: 10.1016/j.marchem.2019.02.003

Luo, Y., Li, G., Xu, W. H., Liu, J. G., Cheng, J., Zhao, J. X., et al. (2021). The effect of diagenesis on rare earth element geochemistry of the Quaternary carbonates at an isolated coral atoll in the South China Sea. *Sediment. Geol.* 420, 105933. doi: 10.1016/j.sedgeo.2021.105933

Luo, Y., Li, G., Xu, W. H., Cheng, J., and Liu, J. (2022). Characteristics of Quaternary exposure surfaces in Well Nanke-1 and their relationship with sea-level changes. *J. Trop. Oceanogr.* 41, 143–157.

Ma, Y. B., Wu, S. L., Lv, F. L., Dong, D. D., Sun, Q. L., Lu, Y. T., et al. (2011). Seismic characteristics and development of the Xisha carbonate platforms, northern margin of the South China Sea. *J. Asian Earth Sci.* 40, 770–783. doi: 10.1016/j.jseaes.2010.11.003

Martin, J. B. (2017). Carbonate minerals in the global carbon cycle. *Chem. Geol.* 449, 58–72. doi: 10.1016/j.chemgeo.2016.11.029

Martin, G. D., Wilkinson, B. H., and Lohmann, K. C. (1986). The role of skeletal porosity in aragonite neomorphism-Strombus and Montastrea from the Pleistocene Key Largo limestone, Florida. *J. Sediment. Petrol.* 56, 194–203.

McArthur, J. M. (1994). Recent trends in strontium isotope stratigraphy. *Terra. Rev.* 6, 331–358. doi: 10.1111/j.1365-3121.1994.tb00507.x

McArthur, J. M., Howarth, R. J., and Bailey, T. R. (2001). Strontium isotope stratigraphy: LOWESS version 3: best fit to the marine Sr-isotope curve for 0–509 Ma and accompanying look-up table for deriving numerical age. *J. Geol.* 109, 155–170. doi: 10.1086/319243

McGregor, H. V., and Gagan, M. K. (2003). Diagenesis and geochemistry of Porites corals from Papua New Guinea: Implications for paleoclimate reconstruction. *Geochim Cosmochim Acta* 67, 2147–2156.

Melim, L. A., Swart, P. K., and Maliva, R. G. (2001). "Meteoric and marine-burial diagenesis in the subsurface of Great Bahama Bank," in *Subsurface geology of a Prograding Carbonate Platform Margin, Great Bahama Bank: Results of the Bahamas Drilling Project*. Ed. (Tulsa, OK, USA: R. N. Ginsburg SEPM Society for Sedimentary Geology), 137–161.

Melim, L. A., Westphal, H., Swart, P. K., Eberli, G. P., and Munnecke, A. (2002). Questioning carbonate diagenetic paradigms: evidence from the Neogene of the Bahamas. *Mar. Geol.* 185, 27–53. doi: 10.1016/S0025-3227(01)00289-4

Miller, K. G., Kominz, M. A., Browning, J. V., Wright, J. D., Mountain, G. S., and Katz, M. (2005). The Phanerozoic record of global sea-level change. *Science* 310, 1293–1298. doi: 10.1126/science.1116412

Mujalli, R. G., Hartmann, J., and Börker, J. (2019). Temperature and CO2 dependency of global carbonate weathering fluxes-Implications for future carbonate weathering research. *Chem. Geol.* 527, 118874.

Opdyke, B. N., and Walker, J. C. G. (1992). Return of the coral reef hypothesis: Basin to shelf partitioning of $CaCO_3$ and its effect on atmospheric pCO_2. *Geology* 20, 733–736. doi: 10.1130/0091-7613(1992)020<0733:ROTCRH>2.3.CO;2

Peya, D. (2017). *Dissolution of CaCO3 in the present and glacial ocean: a comparison of the effects of different dissolution parameterizations* (Bremen: University of Bremen).

Pörtner, H. O., Roberts, D. C., Tignor, M. M., Poloczanska, E., Mintenbeck, K., Alegría, A., et al. (2022). *Climate change 2022: Impacts, adaptation and vulnerability*. (Geneva, Switzerland: IPCC).

Prokoph, A., Shields, G. A., and Veizer, J. (2008). Compilation and time-series analysis of a marine carbonate $\delta^{18}O$, $\delta^{13}C$, $^{87}Sr/^{86}Sr$ and $\delta^{34}S$ database through Earth history. *Earth Sci Rev.* 87, 113–133. doi: 10.1016/j.earscirev.2007.12.003

Purkis, S. J., Rowlands, G. P., and Renaud, P. G. (2010). The paradox of tropical karst morphology in the coral reefs of the arid Middle East. *Geology* 38, 227–230. doi: 10.1130/G30710.1

Qu, H. Z., Wang, Z. Y., Yang, H. J., Zhang, Y. F., Yu, H. F., and Wang, X. (2013). Karstification of reef-bank facies carbonate and its control on pore distribution: A case study of Upper Ordovician Lianglitage Formation in eastern Tazhong area, Tarim Basin, NW China. *Petroleum. Explor. Dev.* 40, 592–598. doi: 10.1016/S1876-3804(13)60077-4

Quinn, T. M., and Matthews, R. K. (1990). Post-Miocene diagenetic and eustatic history of Enewetak atoll: model and data comparison. *Geology* 18, 942–945. doi: 10.1130/0091-7613(1990)018<0942:PMDAEH>2.3.CO;2

Rohling, E. J., Yu, J., Heslop, D., Foster, G. L., and Robert, A. P. (2021). Sea level and deep-sea temperature reconstructions suggest quasi-stable states and critical transitions over the past 40 million years. *Sci Adv.* 7, 5319–5326. doi: 10.1126/sciadv.abf5326

Saller, A. H., and Moore, C. H. (1989). Meteoric diagenesis, marine diagenesis, and microporosity in Pleistocene and Oligocene limestones, Enewetak Atoll, Marshall Islands. *Sediment. Geol.* 63, 253–272. doi: 10.1016/0037-0738(89)90135-8

Schlanger, S. O., and Silva, P. S. (1986). Oligocene sea-level falls recorded in mid-Pacific atoll and archipelagic apron settings. *Geology* 14, 392–395. doi: 10.1130/0091-7613(1986)14<392:OSFRIM>2.0.CO;2

Scholle, P. A., and Ulmer-Scholle, D. S. (2003). *A color guide to the petrography of carbonate rocks: grains, textures, porosity, diagenesis*. (Tulsa, Oklahoma, U.S.A.: The American Association of Petroleum Geologists).

Schroeder, J. H., and Purser, B. H. (2012). *Reef Diagenesis* (Berlin Heidelberg: Springer).

Shao, L., Li, Q. Y., Zhu, W. L., Zhang, D. J., Qiao, P. J., and Liu, X. Y. (2017). Neogene carbonate platform development in the NW South China Sea: Litho-, bio- and chemo-stratigraphic evidence. *Mar. Geol.* 385, 233–243. doi: 10.1016/j.margeo.2017.01.009

Suzuki, A., Kawahata, H., Ayukai, T., and Goto, K. (2001). The oceanic CO2 system and carbon budget in the great barrier reef, Australia. *Geophys. Res. Lett.* 28, 1243–1246. doi: 10.1029/2000GL011875

Swart, P. K. (2015). The geochemistry of carbonate diagenesis: the past, present and future. *Sedimentology* 62, 1233–1304. doi: 10.1111/sed.12205

Swart, P. K., and Oehlert, A. M. (2018). Revised interpretations of stable C and O patterns in carbonate rocks resulting from meteoric diagenesis. *Sediment. Geol.* 364, 14–23. doi: 10.1016/j.sedgeo.2017.12.005

Wang, L. R., Yu, K. F., Zhao, H. T., and Zhang, Q. M. (2014). Economic value assessment of coral reefs in the South China Sea. *Trop. Geogr.* 34, 44–49.

Wang, R., Yu, K. F., Jones, B., Wang, Y. H., and Zhao, J. X. (2018). Evolution and development of Miocene "island dolostones" on Xisha Islands, South China Sea. *Mar Geol* 406, 142–158. doi: 10.1016/j.margeo.2018.09.006

Wolf, K. H. (1973). Carbonate sediments and their diagenesis. *Earth-Sci. Rev.* 9, 152–157. doi: 10.1016/0012-8252(73)90088-3

Wu, L., Wang, R., Yu, K. F., Ren, M., Booker, S., Shen, R., et al. (2024). Meteoric diagenesis influenced by East Asian Summer Monsoon: a case study from the Pleistocene carbonate succession, Xisha Islands, South China Sea. *Palaeogeogr. Palaeoclimatol. Palaeoecol.* 633, 111882. doi: 10.1016/j.palaeo.2023.111882

Wu, S. G., Yang, Z., Wang, D., et al. (2014). Architecture, development and geological control of the Xisha carbonate platforms, northwestern South China Sea. *Mar. Geol.* 350, 71–83. doi: 10.1016/j.margeo.2013.12.016

Xu, S., Yu, K., Fan, T., Jiang, W., Wang, R., Zhang, Y., et al. (2019). Coral reef carbonate δ13C records from the northern South China Sea: a useful proxy for seawater δ13C and the carbon cycle over the past 1.8 Ma. *Global Planet. Change* 182, 103003. doi: 10.1016/j.gloplacha.2019.103003

Yan, H., Shi, Q., Yu, K., Tao, S. C., Yang, H. Q., Liu, Y., et al. (2019). Regional coral growth responses to seawater warming in the South China Sea. *Sci Total. Environ.* 670, 595–605. doi: 10.1016/j.scitotenv.2019.03.135

Yan, H. Q., Yu, K. F., Shi, Q., Tan, Y. H., Liu, G. H., Zhao, M. X., et al. (2016). Seasonal variations of seawater pCO2 and sea-air CO2 fluxes in a fringing coral reef, northern South China Sea. *J. Geophys. Res.: Oceans.* 121, 998–1008. doi: 10.1002/2015JC011484

Yan, H. Q., Yu, K. F., and Tan, Y. H. (2009). Recent development in the research of carbon cycle in coral reef ecosystem. *Acta Ecol. Sin.* 29, 6207–6215.

Yang, Y., Yu, K., Wang, R., Fan, T. L., Jiang, W., Xu, S. D., et al. (2022). 87Sr/86Sr of coral reef carbonate strata as an indicator of global sea level fall: Evidence from a 928.75-m-long core in the South China Sea. *Mar. Geol.* 445, 106758.

You, L., Yu, Y. P., Liao, J., Liu, L., Liu, N., Zhao, S., et al. (2015). Petrological characteristics and pore types of Quaternary reef adjacent typical exposed surface in Well Xike-1, Xisha Islands. *Earth Sci. J China Univ. Geosci.* 4, 6.

Zachos, J. C., Dickens, G. R., and Zeebe, R. E. (2008). An early Cenozoic perspective on greenhouse warming and carbon-cycle dynamics. *Nature* 451, 279–283. doi: 10.1038/nature06588

Zachos, J., Pagani, M., Sloan, L., Thomas, E., and Billups, K. (2001). Trends, rhythms, and aberrations in global climate 65 Ma to present. *Science* 292, 686–693. doi: 10.1126/science.1059412

Zhao, H. W., and Jones, B. (2012). Genesis of fabric-destructive dolostones: A case study of the Brac Formation (Oligocene), Cayman Brac, British West Indies. *Sediment. Geol.* 267-268, 36–54. doi: 10.1016/j.sedgeo.2012.05.007